

# The turbulent/non-turbulent interface at the outer boundary of a self-similar turbulent jet

J. Westerweel, T. Hofmann, C. Fukushima, J.C.R. Hunt

**Abstract** The flow at the outer boundary of a submerged self-similar turbulent jet at  $Re=2\times 10^3$  is investigated experimentally by means of combined particle image velocimetry (PIV) laser-induced fluorescence (LIF) measurements. The jet fluid contains a fluorescent dye so that the LIF data can be used to discriminate between the jet fluid and the ambient fluid. The axial velocity, Reynolds stress, and vorticity are determined relative to the jet boundary. The results are compared against the conventional profiles, and the results of a direct numerical simulation of the turbulent far-wake behind a flat plate. The results show a sharp transition between rotational and irrotational fluid at the fluid interface, and the existence of a layer of irrotational velocity fluctuations outside the turbulent region.

## Introduction

Free turbulent flows, such as wakes, mixing layers, and jets, are bounded by regions of irrotational fluid. The interface between the turbulent and non-turbulent fluid is usually very sharp. The interface is continuously deformed by the turbulent flow, so it has a strongly contorted shape over a wide range of scales. The sharp interface is in strong contrast to the mean flow properties, which show a very gradual change from the turbulent to the non-turbulent flow region. This gradual change is the result of intermittency, in which turbulent and non-turbulent flow regions pass along a fixed point. Bisset et al. (2002) analyzed the flow properties in relation to the instantaneous position  $y_i$  of the interface.

They used a direct numerical simulation (DNS) of the far wake of a parallel flat plate to investigate in detail the turbulent/non-turbulent interface, and how its properties can be related to the outward propagation of the interface.

There is a wealth of visualization studies that describe the structure of the interface between turbulent and non-turbulent regions, but these fail to capture any quantitative information on the turbulence properties. Most experimental descriptions of the turbulent/non-turbulent interface are based on single-point measurement techniques. For example, Chen and Blackwelder (1978) used a heated wall to slightly increase the temperature of the turbulent flow, which could be distinguished from (cooler) non-turbulent fluid using an array of cold wires. The same approach was followed by LaRue and Libby (1974) to study the wake of a heated cylinder. Although the method of using temperature as a passive marker makes it possible to detect whether the probe is in a turbulent or non-turbulent region, it is not able to determine accurately the interface position and measure simultaneously the detailed flow field with high spatial resolution.

These difficulties are overcome by combining two measurement techniques, i.e., laser-induced fluorescence (LIF) and particle image velocimetry (PIV), as is demonstrated in this paper. The measured flow is a submerged self-similar turbulent jet at a Reynolds number  $Re=2\times 10^3$ . A fluorescent dye (fluorescein) is added to the jet fluid, which makes it possible to discriminate between the turbulent (viz., rotational) “jet fluid” and non-turbulent (viz., irrotational) “ambient fluid”. The instantaneous concentration field measured with LIF is used to define the turbulent/non-turbulent interface. The velocity field is determined from the motion of very small tracer particles by means of PIV.

The flow facility and the experimental configuration are described in Sect. 2. The data reduction and the detection of the interface are explained in Sect. 3, and the results are presented in Sect. 4. A summary of the main conclusions is given in Sect. 5.

## 2 Measurements

The details of the flow facility, the experimental conditions and the optical configuration are described in detail by Fukushima et al. (2000). Therefore, this section only describes the features that are relevant to the present investigation. A schematic of the experimental configuration is shown in Fig. 1.

---

Accepted: 12 April 2002  
Published online: 3 August 2002  
© Springer-Verlag 2002

J. Westerweel (✉), J.C.R. Hunt  
Laboratory for Aero and Hydrodynamics,  
Delft University of Technology,  
Leeghwaterstraat 21,  
2628 CA Delft, The Netherlands  
E-mail: j.westerweel@wbmt.tudelft.nl

T. Hofmann  
Departemente für Mathematik und Physik,  
ETH-Zürich, Switzerland

C. Fukushima  
Department of Mechanical and Systems Engineering,  
Gifu University, Gifu, Japan

The authors would like to thank Dr. D.K. Bisset for his suggestions on the investigation presented in this paper.

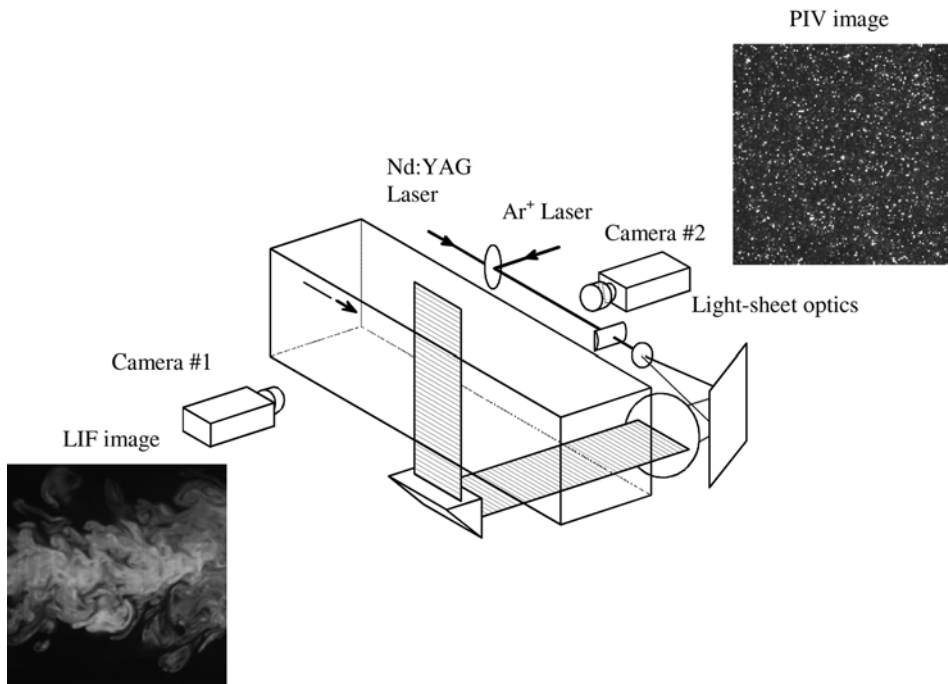


Fig. 1. Schematic of the experimental configuration. From Fukushima et al. (2000)

The measurements are carried out in a rectangular  $110 \times 110 \times 300\text{-mm}^3$  test section. The fluid in the test section and the jet fluid is water at room temperature, which has a kinematic viscosity of  $1.0 \text{ mm}^2/\text{s}$ . The jet fluid enters the test section through a narrow tube (nozzle) with an inner diameter  $d$  of  $1 \text{ mm}$ . The mean velocity in the tube is  $2 \text{ m/s}$ , so that the Reynolds ( $Re$ ) number of the jet is  $2 \times 10^3$ . This value was chosen to match the flow conditions of a DNS by Boersma et al. (1998). The jet fluid is marked with fluorescein, which is a common fluorescent dye. This dye has a Schmidt ( $Sc$ ) number of 2,075, so that the molecular diffusion of the dye is negligible with respect to the turbulent mixing of the jet with the ambient fluid. This means that the boundary of the jet fluid does not become blurred by the effect of molecular diffusion. The fluid is seeded with  $5\text{-}\mu\text{m}$  tracer particles (Durcal) which have a specific gravity of 2.5. The particles are not neutrally buoyant, but due to their small size, they are maintained in homogeneous suspension by the effect of Brownian motion.

A planar cross section of the test section is illuminated with a light-sheet. The light-sheet has a thickness of less than  $1 \text{ mm}$  over a width of  $50 \text{ mm}$ , and consists of the light from two lasers. The first laser is a CW  $\text{Ar}^+$  laser with a total output power of  $5 \text{ W}$ , and the second laser is a twin frequency-doubled pulsed Nd:YAG laser with an energy of  $200 \text{ mJ/pulse}$  and a repetition rate of  $15 \text{ Hz}$ . The  $\text{Ar}^+$  laser is used for the LIF measurements, and the twin Nd:YAG laser for the PIV measurements. The  $\text{Ar}^+$  laser is fitted with an etalon so that it only emits the  $488 \text{ nm}$  (viz., blue) light with a power of  $2.4 \text{ W}$ , and an electro-optical shutter in the laser beam determines the duration of the laser exposure. The beams of the two lasers are combined along the same optical path.

The PIV and LIF images are recorded by two identical digital cameras (Kodak ES 1.0) on opposite sides of the light sheet, with their optical axes perpendicular to the

light-sheet plane (see Fig. 1). The cameras have a spatial resolution of  $992 \times 1,004$  pixels, and a framing rate of  $30 \text{ Hz}$ . The cameras are fitted with identical lenses with a  $55\text{-mm}$  focal length (Micro Nikkor, Nikon). The image magnification is  $0.27$ , and the field-of-view corresponds to a  $45 \times 45 \text{ mm}^2$  area. The center of this area is located at a distance of  $80$  times the jet nozzle diameter. The misalignment between the cameras is less than  $3$  pixel, which corresponds to about  $130 \text{ }\mu\text{m}$  in the object domain.

The first camera records the fluorescent light emitted by the dye. The fluorescent dye has an absorption curve with a maximum near the wavelength of the  $488\text{-nm}$  (blue) light from the  $\text{Ar}^+$  laser, and it emits green light with a maximum intensity at  $514 \text{ nm}$  near the  $532 \text{ nm}$  (green) light of the Nd:YAG laser. An optical filter is placed in front of the camera that transmits the fluorescent light and rejects the  $488\text{-nm}$  (blue) light that is scattered from the tracer particles, so that the recorded intensity represents only the fluorescent light. The duration of the  $\text{Ar}^+$ -laser exposure is  $2.4 \text{ ms}$ . This is a compromise between an exposure long enough to record intensity variations that cover the full gray-level range, and short enough to avoid serious blur due to motion near the jet centerline.

The second camera records the light that is scattered by the tracer particles. The camera is operated in dual-frame mode, so that the two laser exposures are recorded in separate frames. The time delay between the laser pulses is  $1.2 \text{ ms}$ , which is chosen in correspondence to the so-called one-quarter rule for the in-plane displacement (Keane and Adrian 1992) near the jet centerline. In order to avoid exposure of the LIF camera during the PIV recording, and vice versa, the LIF recording is taken with a small time delay directly following the PIV recording, and electro-optical shutters fitted to the cameras avoid unwanted exposure. The total exposure has a duration of  $5 \text{ ms}$ , which is

negligible with respect to the Kolmogorov time scale (20 ms) of the turbulent flow; see Fukushima et al. (2000).

The measurements that are used for the analysis in this paper were taken at a distance of 80 mm from the tube exit. The data presented in this paper are based on one series of 67 combined LIF/PIV measurements. The recording period covers 4.4 s which corresponds to about 150 integral time scales of the turbulent jet (based on the mean half jet width  $b$  and mean centerline velocity  $U_c$ ). The images were recorded with an image acquisition system that consists of two pipeline processors (Datacube MV-200). The total number of measurements in one series is limited by the 256-Mb real-time storage capacity of the image acquisition system. Both cameras had to be operated in so-called dual-frame mode, so each combined measurement comprises four frames: two frames for the PIV measurement, and two frames for the LIF measurement, of which only the second LIF frame contains data.

### 3 Data reduction

The amount of light that is emitted by the fluorescent dye is directly proportional to the intensity of the illumination and the local concentration of the dye, provided the dye concentration is sufficiently low to avoid attenuation of the illumination due to absorption (Walker 1987). The illumination is not homogeneous, so that the LIF images have to be normalized against the intensity profile of the illumination. For this purpose, the test section was filled with a known homogeneous concentration of dye, so that the intensity distribution represents the intensity profile. Also images without illumination are recorded, which represent the dark background level. The LIF images and normalization images are corrected for the background level, and then the corrected LIF images are divided by the corrected normalization image, so that the resultant images represent actual concentration levels. Further details of the normalization procedure are given by Fukushima et al. (2000). It is estimated that the level of precision for the measured instantaneous concentration level is about 1–3%.

The PIV frames pairs are interrogated with a two-pass interrogation procedure using  $32 \times 32$ -pixel interrogation regions and a  $16 \times 16$ -pixel spacing, i.e., each PIV frame pair yields  $(61 \times 61 =) 3,721$  velocity vectors. The result from the first pass is used to determine the window off-set for the second interrogation pass (Westerweel et al. 1997). The fraction of spurious vectors is less than 2%, which could be reliably detected by means of a median test (Westerweel 1994) and were replaced by linear interpolation. The instantaneous field for  $\Omega_z$ , i.e., the vorticity component perpendicular to the light-sheet plane, was determined from the instantaneous velocity field by means of the circulation method described by Reuss et al. (1989). The precision of the displacement measurements is estimated at 0.1 pixel, which is a precision of better than 4 mm/s for the velocity.

A typical example of a combined LIF/PIV measurement is shown in Fig. 2, where the instantaneous velocity field measured with PIV is superimposed on a false-color rendering of the instantaneous concentration field measured

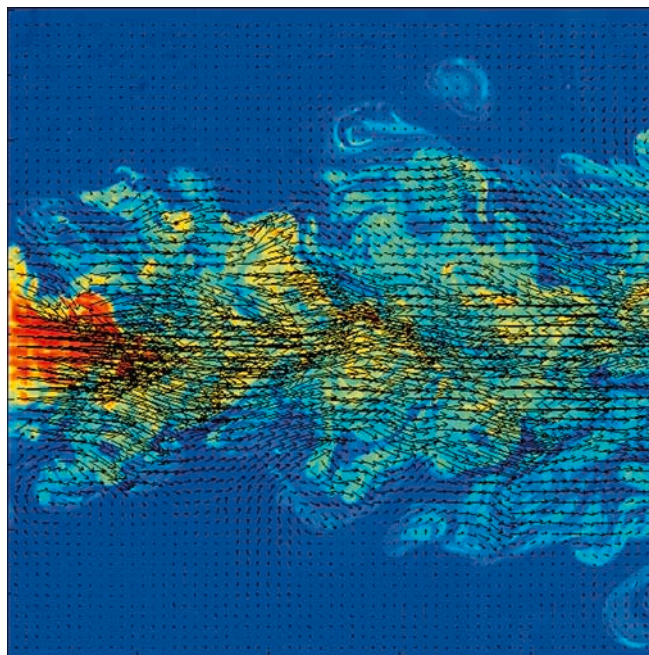


Fig. 2. Result of a combined LIF/PIV measurement

with LIF. It should be noted that the magnitude of the vectors is exaggerated in order to show the correspondence of the concentration and velocity data in the outer region of the jet. The LIF results are used to define the interface between the jet fluid and the ambient fluid. The different stages of detection of the jet interface are illustrated in Fig. 3, and described below.

The LIF data are transformed into binary images by means of threshold detection: pixels with a gray value above the threshold value are labeled “1” (i.e., jet fluid),

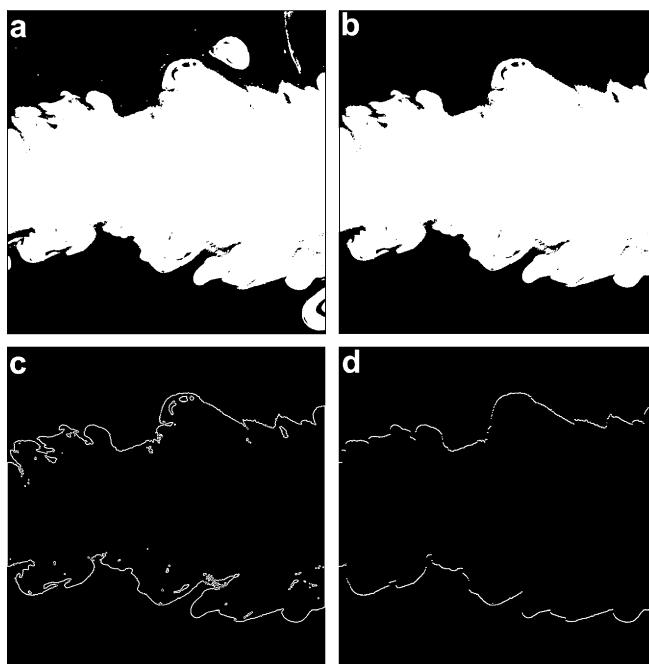


Fig. 3. The detection of the outer boundary of the jet (*see text*)

and all other pixels are labeled “0” (i.e., ambient fluid). The threshold value is chosen in accordance with the procedure described by Prasad and Sreenivasan (1989), which is based on a graph of the mean concentration of all pixels above the threshold value as a function of the threshold value. The graph for the LIF result in Fig. 2 is shown in Fig. 4. The curve has two (nearly) linear regions, which are indicated by the fitted dashed lines in Fig. 4. It should be noted that prior to the threshold detection, a median filter was applied to the concentration field in order to remove single-pixel objects in the background; it was found that such objects were the occasional (weak) images of tracer particles that scatter the (green) fluorescent light (which is transmitted by the optical filter) and that are large enough to leave an image on the camera sensor.

The binary image in Fig. 3a shows that the jet may contain regions of entrained “ambient fluid”, which appear as “holes” in the jet, and regions of detrained “jet fluid”, which appear as “islands” outside the jet. Each object is labeled, and all objects that are not connected to the centerline of the jet are removed (Fig. 3b). The remaining object is eroded, which is a morphological operation that removes all pixels connected to the object

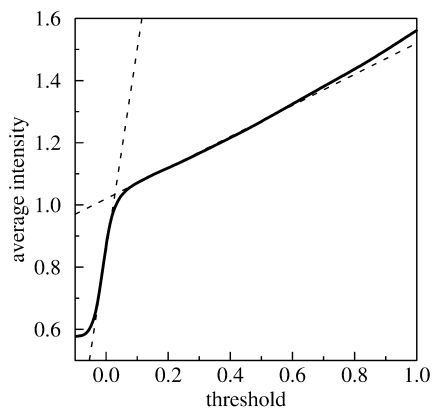


Fig. 4. Selection of the detection threshold for the jet fluid using the method of Prasad and Sreenivasan (1989). The dashed lines intersect at a threshold value of 0.03

exterior (Jain 1989). The object boundary is then obtained as the result of an exclusive or (XOR) of the original and eroded binary images; see Fig. 3c. The result is a 1-pixel-thick continuous curve that represents the jet boundary. The shape of the interface can be quite complex, i.e., in some places a vertical line can intersect the interface more than once. This complicates the further analysis of the data, and therefore it was decided to filter the interface by saving the outmost points of the interface along each vertical line. The result is shown in Fig. 3d. This final operation can cause “discontinuities” in the interface, and it affects the ability of the analysis to reveal small-scale structures. However, the present analysis is aimed at revealing the large-scale structure, for which such minor errors in the interface are considered to be negligible.

Once the outer jet interface is determined, the flow statistics can be determined relative to the position  $y_i$  of the interface. The velocity data are interpolated on a grid with a  $1 \times 1$ -pixel spacing to match the resolution of the LIF data, and the conditional statistics for the axial velocity, Reynolds stress, and vorticity over a range from  $-300$  pixel to  $+300$  pixel on either side of the boundary. In Fig. 5a, the interface in Fig. 3d is superimposed on the (interpolated) vorticity field of the velocity field in Fig. 2. In Fig. 5b and c, the same data are plotted, but now relative to the upper and lower jet interfaces. The results for the velocity, Reynolds stress and vorticity are determined by taking averages along horizontal lines in Fig. 5b and c, and by averaging these data over all combined LIF/PIV measurements.

#### 4 Results

The conventional flow statistics with respect to the (fixed) jet centerline are determined by taking averages along lines parallel to the jet centerline, i.e.,  $y=0$ . The self-similar shape would dictate an averaging along polar lines with constant  $y/x$ , but the present data are taken at  $x/d=60-100$ , where the spreading of the jet is quite small. So, the error by averaging along parallel lines is considered to be negligible. The mean centerline velocity  $U_c$  of the jet is  $183$  mm/s, and the jet half-width  $b$  is  $5.2$  mm. Both  $U_c$  and  $b$  are obtained by fitting a Gaussian curve to the profile of

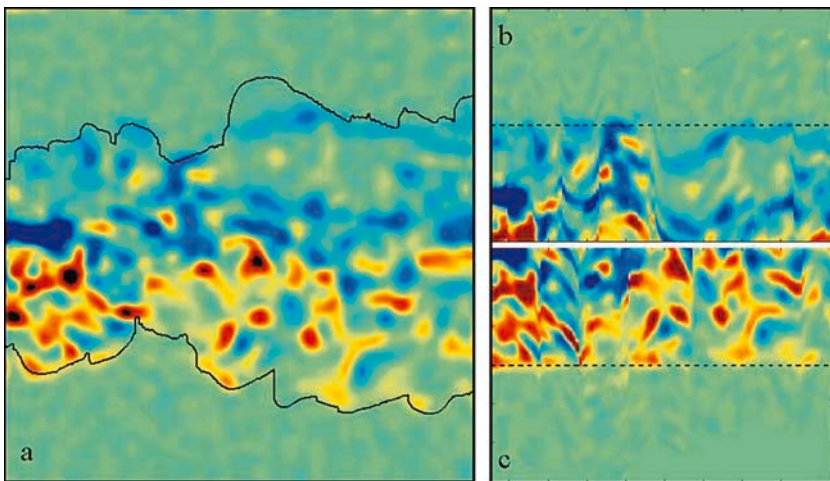


Fig. 5. a The vorticity  $\Omega_z$  and jet outer boundary (continuous line). b The vorticity relative to the upper boundary (dashed line). c The vorticity relative to the lower boundary

the mean axial velocity  $\bar{U}(y)$  and are used for presenting the results in non-dimensional form. The profiles for  $\bar{U}(y)$ , the turbulence intensities  $u'$  and  $v'$  of the axial and radial velocity fluctuations respectively, and the Reynolds stress  $\bar{uv}$  are plotted in Fig. 6. Also included in these graphs are the corresponding results from the DNS by Boersma et al. (1998), which shows a good correspondence between the experimental and numerical results. A more detailed comparison of the experimental and numerical data is presented by Fukushima et al. (2000).

The graph in Fig. 5a shows the interface contour superimposed on the instantaneous vorticity (viz.,  $\Omega_z$ ). The blue and red regions indicate regions of strong positive and negative vorticity respectively. This graph clearly shows that the flow outside the jet boundary is irrotational (viz.,  $\Omega_z=0$ ). This is made even more apparent by plotting the data relative to the interface, as shown in Fig. 5b and c. The dashed lines correspond to the upper and lower solid curves in Fig. 5. It should be noted that there appear to be some regions just within the detected interface where the vorticity vanishes, but which belong to the jet fluid (e.g., below the bulge in the center of the upper interface in Fig. 5a). These may represent regions of detained jet fluid. This will affect the results for the flow statistics relative to the jet boundary. In the case of vorticity

statistics, the contribution to the sum is practically zero, so that the effect will be a reduction in the mean level for the conditionally averaged statistics.

The solid curves in Fig. 5a define the upper and lower interface contours, denoted by  $y_i(x)$ , which is used to determine the flow statistics relative to the interface. The results for the conditional statistics of the axial velocity  $\langle U \rangle$ , the Reynolds stress  $\langle uv \rangle$ , and the vorticity  $\langle \Omega_z \rangle$  are plotted in Fig. 7. For comparison, the results for the conventional statistics, shifted over a distance  $2b$ , are also plotted in Fig. 7. The data for the mean vorticity were obtained by differentiation of  $\bar{U}(y)$ . The data clearly show that the interface separates rotational and irrotational fluid. This is most clearly visible in the result for  $\langle \Omega_z \rangle$ , where the mean vorticity level has a constant value of about  $0.5 U_c/b$  for  $y < y_i$  and vanishes for  $y > y_i$ . This region of constant vorticity corresponds to a linear profile for  $\langle U \rangle$ , i.e.,  $\langle U \rangle = -0.5 U_c (y - y_i) / b$  for  $y < y_i$ . The result for the Reynolds stress shows that  $\langle uv \rangle$  does not vanish at the interface, but at a distance of about  $0.6 - 1.0b$ . This indicates the presence of irrotational velocity fluctuations outside the interface.

The distance between the symbols in Fig. 7 corresponds to a 16-pixel spacing, and is representative for the spatial resolution of the PIV data. For  $\langle U \rangle$  and  $\langle uv \rangle$ , the smallest

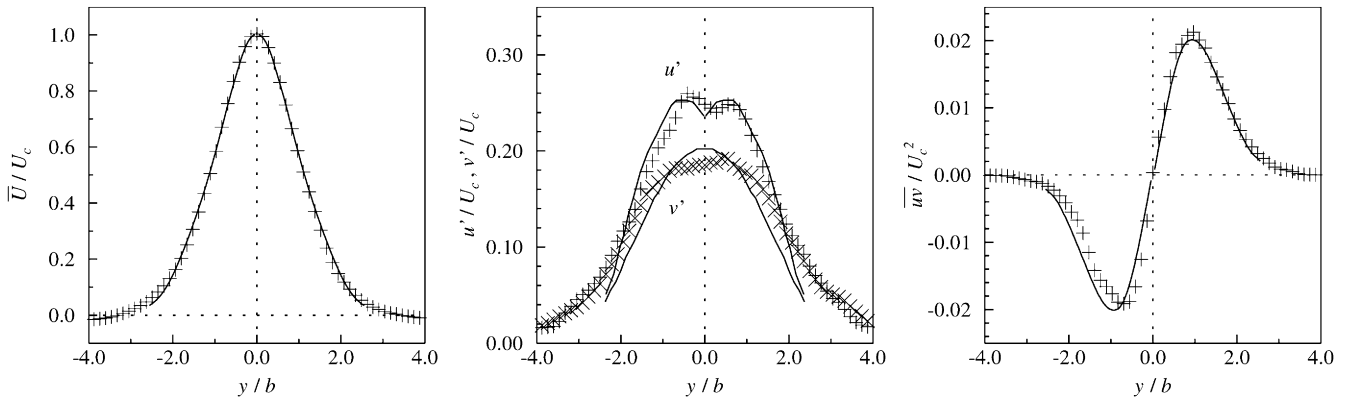


**Fig. 6.** The radial profiles for the mean axial velocity  $\bar{U}$ , axial  $u'$  and radial  $v'$  turbulence intensities, and Reynolds stress  $\bar{uv}$ , relative to the mean centerline velocity  $U_c$  and jet half-width  $b$ . Symbols represent

present data; *solid lines* represent results from the DNS of Boersma et al. (1998)

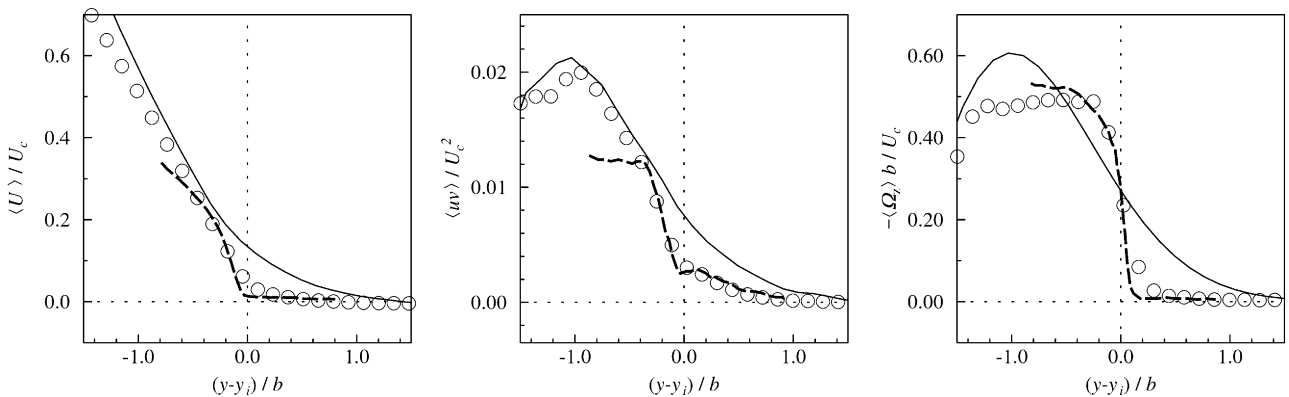


**Fig. 7.** The mean axial velocity  $\langle U \rangle$ , Reynolds stress  $\langle uv \rangle$ , and vorticity  $\langle \Omega_z \rangle$  as functions of the distance from the interface at  $y_i$ , relative to the mean centerline velocity  $U_c$  and jet half-width  $b$  (*open*

*circles*, present data relative to interface; *solid lines*, present data relative to fixed position  $y=2b$ ; *broken lines*, scaled results from DNS data from Bisset et al. (2002)

spatial scales that can be resolved correspond to the size of the interrogation domain, i.e., 32 pixels (the distance to every second data point in Fig. 7). The vorticity is computed by means of the circulation method (Reuss et al. 1989), which involves a contour along 3×3 interrogation positions in the PIV data. This contour includes a 32×32-pixel region in the image, but uses PIV data that cover a 64×64-pixel domain. Hence, a conservative estimate of the spatial resolution for the profile of  $\langle \Omega_z \rangle$  is that it encloses five data points. Note that this is also the number of data points over which the vorticity drops to zero when crossing the interface. Hence, the rate at which the vorticity drops to zero in Fig. 7 is limited by the spatial resolution of the data, and the width of the region in Fig. 7 should be considered as an upper limit for the thickness of the interface. It is expected that interrogation of the PIV data with smaller interrogation domains will show a sharper transition between the rotational and irrotational domains.

In Fig. 7, the corresponding results of a DNS for a turbulent wake behind a parallel plate are also included (Bisset et al. 2002). It should be noted that the scaling of the DNS profiles was adapted to find a proper matching with respect to the present experimental results. This implies that the centerline velocity and half-width are not the proper (universal) scaling parameters for the turbulent/non-turbulent interface. This is not surprising, given the fact that the DNS data and experimental data represent quite different flows. There is a good agreement between the experimental and numerical results, in particular for the Reynolds stress. Also the results for the vorticity compare quite well, although Bisset et al. (2002) considered the vorticity magnitude, i.e.,  $\langle |\Omega_z| \rangle$ .

## 5 Conclusions

Combined LIF/PIV measurements in the far field of a submerged self-similar turbulent jet are used to investigate the motion with respect to the interface between the jet fluid and the ambient fluid. It was demonstrated by Fukushima et al. (2000) that the jet flow is self-similar. The subset of data used for the present analysis is in good agreement with the results from a DNS of a turbulent jet at the same Reynolds number (Fig. 6). The procedure of Prasad and Sreenivasan (1989) was used to detect the interface.

The results in Figs. 5 and 7 show that the flow outside the interface can be considered as irrotational with a constant mean level of vorticity inside the interface. The Reynolds stress has a finite level at the interface which indicates the presence of irrotational velocity fluctuations in a region outside the interface. The results from the present experimental data strongly resemble the corresponding results obtained by Bisset et al. (2002) from a DNS of a turbulent wake behind a parallel plate.

The turbulent/non-turbulent interface is very sharp, and for the present data it seems that the observed width is

primarily determined by the finite spatial resolution of the PIV data. It was observed that the PIV analysis based on 32×32-pixel interrogation domains produces a very low level of spurious measurement data. Allowing a higher – but still very acceptable – level of spurious data would make it possible to reduce the interrogation domain to 16×16 pixels. Also under consideration is the tracking of individual tracer particles close to the interface, which would maximize the spatial resolvability of the present data. This would make it possible to reduce the experimental value for the upper limit of the thickness of the interface.

To simplify the analysis, only the outermost points of the detected interface were kept (see Fig. 3), and thus some of the detailed contorted structure of the interface was lost. Also, the flow properties relative to the interface position were determined only in the radial direction, without regard for the orientation of the interface. Most likely, the result of these simplifications is a loss of the small-scale behavior in the vicinity of the interface, and thus the results presented in Fig. 7 reflect the large-scale structure only. The development of an analysis program that can handle a contorted interface and that takes into account the orientation of the interface is currently under development.

## References

- Bisset DK, Hunt JCR, Rogers MM (2002) The turbulent/non-turbulent interface bounding a far wake. *J Fluid Mech* 451:383–410
- Boersma BJ, Brethouwer G, Nieuwstadt FTM (1998) A numerical investigation on the effect of the inflow conditions on the self-similar region of a round jet. *Phys Fluids* 10:899–909
- Chen CHP, Blackwelder RF (1978) Large-scale motion in a turbulent boundary layer: a study using temperature contamination. *J Fluid Mech* 89:1–31
- Fukushima C, Aanen L, Westerweel J (2000) Investigation of the mixing process in an axisymmetric turbulent jet using PIV and LIF. Paper presented at the 10th International Symposium on Applications of Laser Techniques to Fluid Mechanics, Lisbon, Portugal, 10–13 July, paper 11-1
- Jain AK (1989) *Fundamentals of digital image processing*. Prentice Hall, Englewood Cliffs, N.J.
- Keane RD, Adrian RJ (1992) Theory of cross-correlation analysis of PIV images. *Appl Sci Res* 49:191–215
- LaRue JC, Libby P (1974) Temperature fluctuations in the plane turbulent wake. *Phys Fluids* 17:1956–1967
- Prasad RR, Sreenivasan KR (1989) Scalar interfaces in digital images of turbulent flows. *Exp Fluids* 7:259–264
- Reuss DL, Adrian RJ, Landreth CC, French DT, Fansler TD (1989) Instantaneous planar measurements of velocity and large-scale vorticity and strain rate in an engine using particle-image velocimetry. SEA Technical Paper 890616
- Walker DA (1987) A fluorescent technique for measurement of concentration in mixing liquids. *J Phys E* 20:217–224
- Westerweel J (1994) Efficient detection of spurious vectors in particle image velocimetry data. *Exp Fluids* 16:236–247
- Westerweel J, Dadvini D, Gharib M (1997) The effect of a discrete window offset on the accuracy of cross-correlation analysis of digital PIV recordings. *Exp Fluids* 23:20–28